



HAL
open science

Experimental and numerical investigation of biosensors plasmonic substrates induced differences by e-beam, soft and hard UV-NIL fabrication techniques

Jean-François Bryche, Frédéric Hamouda, Mondher Besbes, Philippe Gogol, Julien Moreau, Marc Lamy de La Chapelle, Michael Canva, Bernard Bartenlian

► To cite this version:

Jean-François Bryche, Frédéric Hamouda, Mondher Besbes, Philippe Gogol, Julien Moreau, et al.. Experimental and numerical investigation of biosensors plasmonic substrates induced differences by e-beam, soft and hard UV-NIL fabrication techniques. *Micro and Nano Engineering*, 2019, 2, pp.122-130. 10.1016/j.mne.2018.11.003 . hal-02184340

HAL Id: hal-02184340

<https://hal.science/hal-02184340>

Submitted on 15 Jul 2019

HAL is a multi-disciplinary open access archive for the deposit and dissemination of scientific research documents, whether they are published or not. The documents may come from teaching and research institutions in France or abroad, or from public or private research centers.

L'archive ouverte pluridisciplinaire **HAL**, est destinée au dépôt et à la diffusion de documents scientifiques de niveau recherche, publiés ou non, émanant des établissements d'enseignement et de recherche français ou étrangers, des laboratoires publics ou privés.



Research paper

Experimental and numerical investigation of biosensors plasmonic substrates induced differences by e-beam, soft and hard UV-NIL fabrication techniques

J.-F. Bryche^{a,b,d,*}, F. Hamouda^a, M. Besbes^b, P. Gogol^a, J. Moreau^b, M. Lamy de la Chapelle^c, M. Canva^{b,d}, B. Bartenlian^a

^a Centre de Nanosciences et de Nanotechnologies (C2N); CNRS, Univ. Paris-Sud, Université Paris-Saclay; Palaiseau, France

^b Laboratoire Charles Fabry (LCF); Institut d'Optique Graduate School, CNRS, Univ. Paris-Sud, Université Paris-Saclay; Palaiseau, France

^c Institut des Molécules et Matériaux du Mans (IMMM); Le Mans Université; Le Mans, France

^d Laboratoire Nanotechnologies Nanosystèmes (LN2); CNRS, Université de Sherbrooke; 3IT, Sherbrooke, Canada



ARTICLE INFO

Article history:

Received 8 October 2018

Accepted 11 November 2018

Keywords:

Plasmonics

E-beam lithography

Nanoimprint lithography

UV-NIL

SPRI

SERS

ABSTRACT

This paper compares plasmonic substrates manufactured by three lithography methods: E-beam, soft and hard UV NanoImprint Lithography. The different plasmonic modes existing in samples made of an array of gold nanostructures on gold film are investigated for biochemical detections taking advantage of Surface Plasmon Resonance Imaging (SPRI) and Surface-Enhanced Raman Scattering (SERS). Recently, it has been shown that this geometry of substrate is of great interest for both SPRI and SERS measurements. A comparison of their performances obtained by the different lithographic methods is provided. In particular, due to limitations in NanoImprint Lithographic techniques, the impact of sidewall geometry of nanostructures is investigated in regard to plasmonic properties. Thus, experimental optical characterization analyses have been carried out on samples and compared with the numerical simulations.

© 2018 The Authors. Published by Elsevier B.V. This is an open access article under the CC BY-NC-ND license (<http://creativecommons.org/licenses/by-nc-nd/4.0/>).

1. Introduction

Improvement of plasmonic sensors has been linked to nanofabrication processes. Indeed, several biosensing techniques based on nanostructuring to increase the sensitivity and allow the detection of molecules at lower concentrations are widely used: Surface Plasmon Resonance (SPR) [1], Surface-Enhanced Raman Scattering (SERS) [2,3], Surface-Enhanced Infrared Absorption (SEIRA) [4], Surface Plasmon-Enhanced Fluorescence Spectroscopy (SPFS) [5]. Now, biosensor's trend is to combine two or more techniques to take advantage of each. In this way, Mass Spectroscopy (MS) [6], Atomic Force Microscopy (AFM) [7], Surface Acoustic Waves (SAW) [8,9] sensors have been combined with SPR setup. In this work, we focus our studies on a sample used in bimodal instrument combining SPRI and SERS measurement [10–13]. Indeed, such bimodal instrument would allow a real-

time and parallel detection of biomolecular interactions, thanks to SPRI sensor, while SERS would give simultaneously molecular identification linked to vibration modes of the molecules. Many techniques can be used to realize SERS or SPRI nanostructured samples [14] as E-Beam lithography (EBL) [15,16], X-ray interference Lithography [17], Focused Ion beam [18], Nanosphere lithography [19,20]. Among them, Nanoimprint Lithography (NIL) [21,23] is a useful technique to obtain large areas nanopatterned with a relatively low cost for industrial applications. Soft Nanoimprint Lithography assisted by UV (Soft UV-NIL) is a NIL pathway using a flexible polydimethylsiloxane (PDMS) stamp which avoids the constraints related to the inhomogeneity of a substrate thickness and its curvature. Fabrication of gold nanostructures [24,26] by soft UV-NIL is a promising technique used for detection of biochemical molecules. However, for specific dimensions and densities of nanostructures and to get around some effects, such as collapse [27,28] and wettability [29,30], related to the manufacture of the elastomeric mold, Hard UV-NIL [31] can be an alternative technique. In this work, we compared E-beam lithography, Soft and Hard UV-NIL processes for the fabrication of bimodal plasmonic substrates based on a specific pattern of gold nanodisks on gold film. We will compare each

* Corresponding author at: Laboratoire Nanotechnologies Nanosystèmes (LN2); CNRS, Université de Sherbrooke; 3IT, Sherbrooke, Canada.

E-mail address: jean-francois.bryche@usherbrooke.ca (J.-F. Bryche).

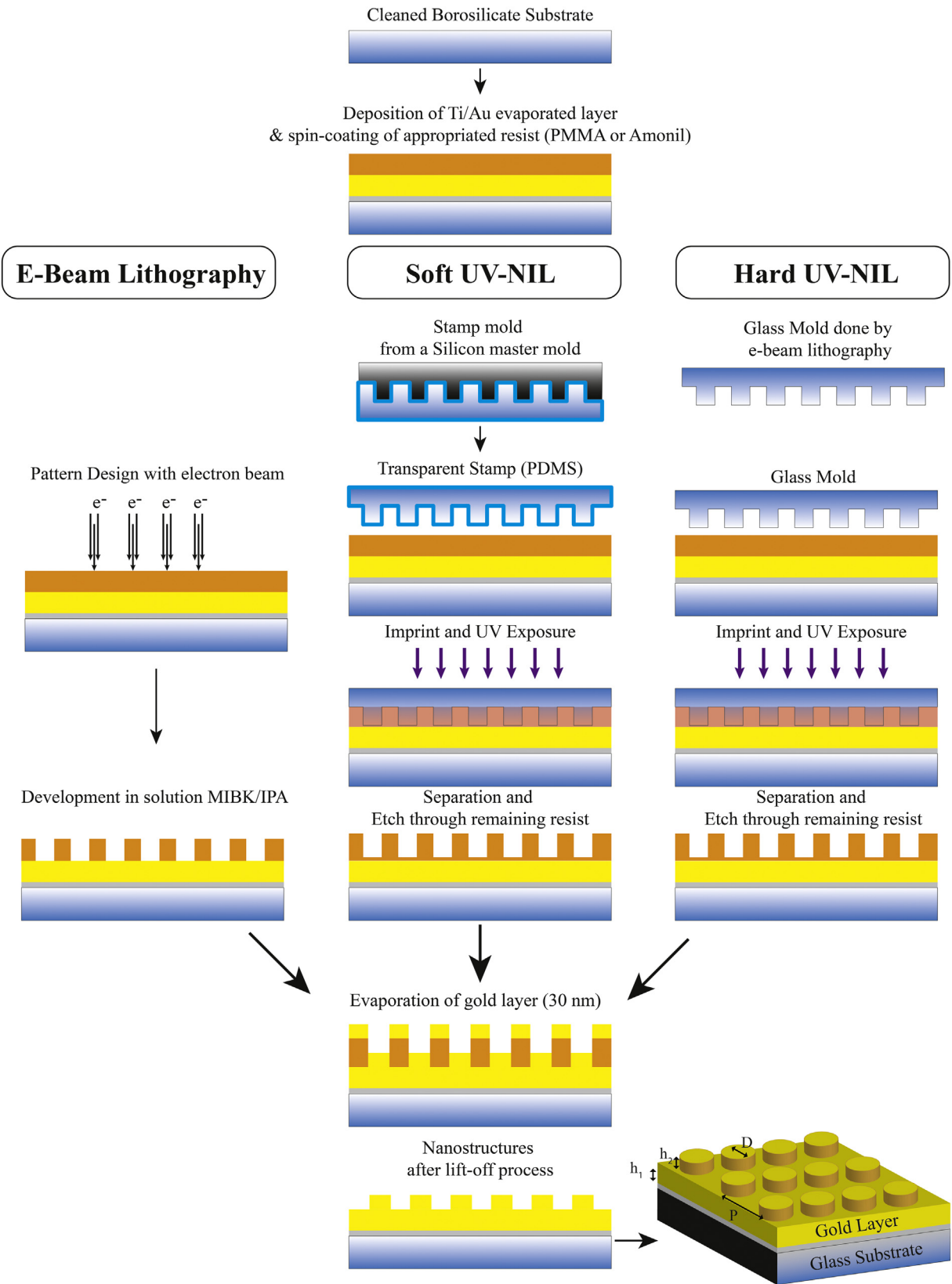


Fig. 1. Scheme of (a) e-beam lithography, (b) soft UV-NIL and (c) hard UV-NIL processes.

technique in terms of SPR and SERS response. Due to the resolution's limits in nanofabrication, the effects of a sidewall of the nanodisks will be comment and related to the plasmonic performances of each substrate.

2. Experimental details

The sample is composed of an array of gold nanodisks on gold film on BK7 glass substrates (Fig. 1). The gold film underlayer is necessary

for SPRI in Kretschmann configuration and also give rise to a new hybrid lattice mode (HLP) [32]. This mode is also responsible for one order of magnitude improvement in SERS enhancement factor (EF) without adding complex step process [33]. For the three techniques detailed in this section, samples are cleaned beforehand in ethanol, acetone and piranha solutions (composed of 3:1 concentrated sulfuric acid to 30% hydrogen peroxide solution). A 2 nm titanium layers followed by a 30 nm gold layer are deposited by e-beam evaporation on the glass substrate. At the end of each process, the gold nanodisks have a height of 30 nm. Fig. 1 describes typical step for e-beam lithography, soft UV-NIL and Hard UV-NIL processes.

2.1. E-beam lithography

Gold nanostructures obtained by E-beam lithography are called e-GNGU (in reference to E-beam lithography of Gold Nanostructures on Gold Underlayer).

The detailed e-beam process has been already reported in previous studies on SERS improvement [33,34]. Major steps are the deposition of a 80 nm resist layer of polymethylmethacrylate A2 (PMMA A2) by spin coating followed by the writing step of e-beam lithography. All samples were realized with a NanoBeam (nB4) system with an accelerating voltage of 80 kV and 2 nA of current. The development of insulated area is performed in 1:3 methylisobutylketone/isopropanol (MIBK/IPA) solution. Finally, a 30 nm gold layer is evaporated and a lift-off process in acetone is done. The e-GNGU structures show good uniformity and homogeneity due to the e-beam process.

2.2. Soft UV-NIL

Gold nanostructures obtained by soft UV-NIL are called s-GNGU (in reference to soft UV-NIL).

2.2.1. Master mold fabrication

The first step for soft UV-NIL is the fabrication of the master mold. A silicon substrate is cleaned by several baths in this order: ethanol, acetone, deionized (DI) water, pure nitric acid, DI water, Hydrofluoric acid (HF) in Ammonium fluoride (NH_4F) (1:4), DI Water, piranha solution and DI water solutions. Next, the pattern (nanodisk array) is designed by e-beam lithography on PMMA spin-coated layer. Reactive Ion Etching (RIE) process has been optimized to transfer the pattern in Si master mold. By changing flow and pressure of SF_6 and C_4F_8 gases and intensity power, i.e. by moving from anisotropic to isotropic etching [35] we can control the slope of hole sides. Another way to obtain

inclined side walls is to use variable dose control of e-beam writing steps with a negative resist as reported in [36]. Indeed, to avoid collapses phenomena of PDMS nanostructures of flexible stamp mold, one way is to have inclined side walls which are more appropriate than vertical side walls due to widened base. Other ways to avoid collapses phenomena is to take care of the ratio between the height and the diameter of the PDMS nanostructures [27]. An elegant study has been done about the stability of bigger structures in PDMS stamps by Navajas et al. [37]. Another advantage to have inclined side walls is to facilitate the unmolding step by decrease stress and shrinkage.

2.2.2. PDMS stamp, print step, Au deposition and lift-off

Before the fabrication of PDMS stamp, Si master mold is cleaned with HF and H_2O_2 solutions to obtain a thin oxide in the surface. Then, an anti-adhesion layer, the Trimethylchlorosilane (TMCS) is used to reduce the surface energy of silicon [38] and make easier the unmolding step of PDMS stamp. The PDMS stamp is done from undiluted PDMS (RTV615) mixed with his curing agent. The PDMS solution is deposited on Si master mold, degassed and cured at 60°C for 24 h. Height and diameter are chosen to have h/d lower than critical aspect ratio equal to 1.47 in our case [27].

The next step is the imprint process with an EVG 620 mask aligner from EV Group (Austria). PDMS stamp is printed in an inorganic UV curable resist AMONIL MMS4 (from AMO GmbH) deposited by spin-coating on the top of a sacrificial PMMA layer. The thickness of Amonil layer is around 120 nm. PMMA layer was used to easily remove AMONIL after the UV curing and to improve range of aspect ratio of nanostructures (by changing PMMA thickness used as etching mask). The conditions of imprint process are a pressure of 400 mbar and a contact time of 2 min before the UV-polymerization of AMONIL resist through the transparent mold. The polymerization is performed with UV exposure at 365 nm wavelength with 2000 mJ. After a quick etching of the residual layer of Amonil and PMMA resist, gold is deposited by evaporation followed by a lift-off process in acetone.

2.3. Hard UV-NIL

Gold nanostructures obtained by Hard UV-NIL are called h-GNGU (in reference to hard UV-NIL).

2.3.1. Master mold fabrication

The UV Hard mold used four levels (Fig. 2, a) with a glass carrier, a thin PDMS layer (20 μm) to ensure soft bonding between BK7 glass

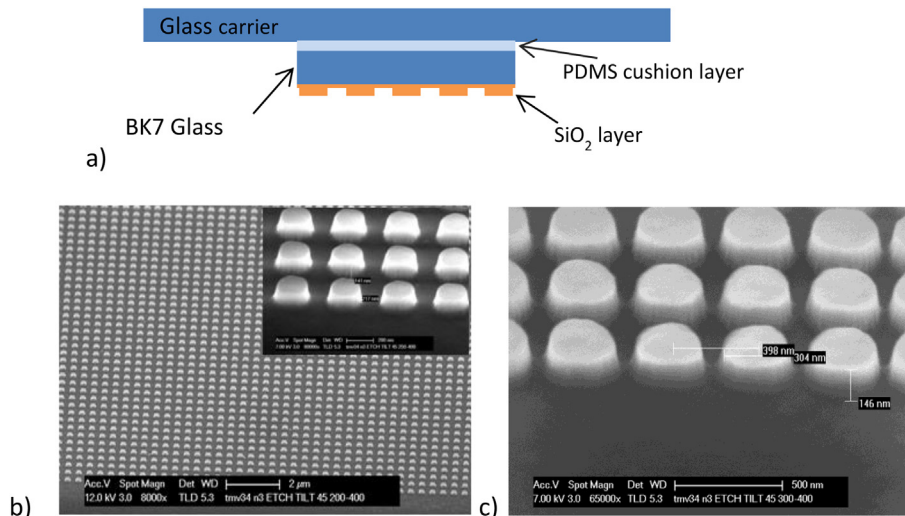


Fig. 2. Scheme of the hard mold for UV-NIL and SEM pictures of the glass master mold after etching process: (b) zone and zoom with $P = 400$ nm and $D = 200$ nm, (c) Other area with $P = 400$ nm and $D = 300$ nm.

substrate (2 cm × 2 cm × 900 μm) and glass carrier [39]. Then a thin layer of SiO₂ (2 μm) was deposited by a plasma-enhanced chemical vapor deposition (PECVD STS) at low frequency, 380 KHz (LF-SiO₂). A 120 nm thick polymethylmethacrylate (PMMA A4) resist baked at 175 °C during 10 min was used for the EBL process in order to obtain nanostructures. A lift-off process is realized with a 30 nm chromium deposited by e-beam evaporation.

The etching process of the LF-SiO₂ was performed by a RIE equipment with SF6 gas (200 sccm gas flow, 8 mTorr working pressure, 70 W). After it, a dry etching was used to remove the chromium mask. The final structure height was 190 nm observed with a SEM, as illustrated in Fig. 2 (b and c). In the same way than soft UV-NIL process, before imprint process, the fluorinated anti-sticking layers (ASLs) was deposited in liquid phase to reduce the surface energy. The products used for the ASLs process were 1H, 1H,2H,2H-Perfluorooctyltrimethoxysilane (F13-TMS) from ABCR and perfluorohexane from ALFA AESAR. The treatment has been detailed in the reference [40]. Measuring the surface energy with contact angle confirms the efficiency of the treatment, as it went from 47 mN/m to 12 mN/m after ASLs. Hard UV-NIL was performed with the same inorganic UV curable resist from AMO GmbH and the sacrificial layer Polymethylmethacrylate (PMMA A10). The resists were deposited on glass substrate previously cleaned and covered with a 2 nm Ti and 30 nm Au layers. The printing conditions are similar to the Soft UV-NIL with a pressure of 900 mBar, higher than with soft UV-NIL. This pressure can play a key role to obtain close patterns (high density of nanodisks) or to reduce critical size.

Etch process of the AMO residual layer and PMMA A10 sacrificial resist used for the pattern transfer has been described in the reference [14] and stopped at the level of gold film (Fig. 3). An Au layer (30 nm) is evaporated on this gold film and the remaining AMONIL/PMMA bilayer was removed by a lift-off process. A certain roughness around the disks is attributed to the RIE process of the glass master mold, visible in the Amonil imprint (Fig. 3 b, insert).

3. Results and discussion

We present different characterizations of plasmonic substrates fabricated with these three lithographic methods: E-beam, Soft, and Hard UV-NIL.

For each method, nanostructures have been observed by SEM (Fig. 4). As expected, nanodisks realized by e-beam lithography are well-defined and show a low roughness. On the contrary, nanodisks done by soft and hard UV-NIL show a higher roughness linked to the roughness obtained respectively with the silicon master mold and the glass mold during the RIE process. Thanks to the stamps in PDMS and its viscoelasticity, this roughness defect is minored for s-GNGU sample.

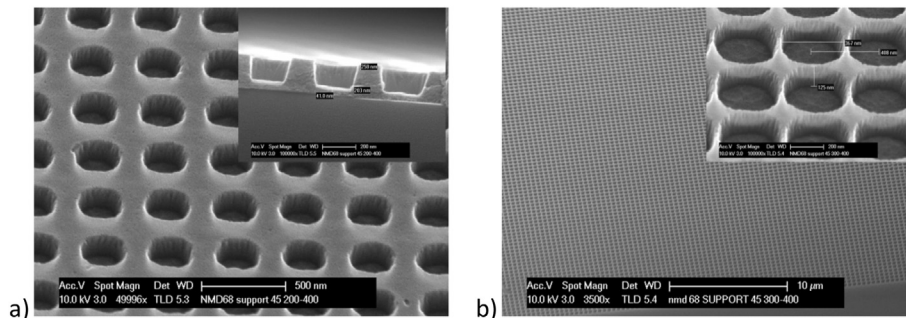


Fig. 3. SEM pictures of the imprint in AMONIL resist without PMMA A10 45° tilted and his cross-section in zoom: (a) P = 400 nm and D = 200 nm, (b) D = 300 nm for second area.

3.1. Optical characterization results

3.1.1. SPRI Measurements

Nanostructures shown in Fig. 4 were characterized by SPRI system based on a Kretschmann configuration previously reported [41]. Fig. 5 shows normalized angulo-spectral SPR reflectivity map of the sample (TM reflectivity, P polarization divided by TE reflectivity, S polarization) in water solution for e-GNGU sample (D = 50 nm, P = 300 nm). Data showed are interpolated by cubic method. Several reflectivity dips can be observed and correspond to resonances of plasmonic modes.

In presence of a continuous gold film, a propagative surface plasmon (SPP) mode can occur and be described by the wave vector ($k_{spp} = \frac{\omega}{c} \sqrt{\frac{\epsilon_m \epsilon_d}{\epsilon_m + \epsilon_d}}$) with the approximation of semi-infinite system. ϵ_m and ϵ_d correspond respectively to the dielectric permittivity of the metal and the surrounding dielectric media. Due to the periodicity of nanostructures, this wave vector k_{spp} can be coupled to lattice vector $\frac{2\pi}{P}$ known as Wood-Plasmon anomalies (WP). “m” correspond to the order of diffraction of the array of period P.

$$k_{wp} = k_{spp} \pm m \times \frac{2\pi}{P} \tag{1}$$

Moreover, the nanostructures themselves can support localized surface plasmon (LSP) mode as a function of several geometrical parameters (diameter and period). In our structures, these two plasmonic modes can coexist. Each time the wave vectors of these modes are equal, a phenomenon of band-gap or so call anticrossing is observed on the reflectivity map. As describe in Reference [42], a coupling between two oscillators modes can occur as observed and confirmed experimentally [30, 41] for two plasmonic modes. In the hypothesis of a weak coupling, the two branches of the wave vector of this hybrid mode is described as [42,44]:

$$k_{hybrid\pm} = \sqrt{\frac{1}{2} \times \left[k_{spp}^2 + k_{lsp}^2 \pm \sqrt{(k_{spp}^2 - k_{lsp}^2)^2 + 4 \times \frac{\Gamma^2}{c^2}} \right]} \tag{2}$$

Γ corresponds to a coupling parameter. An example of simulated map is presented in Fig. 5 on a structure with well chosen parameters to illustrate this coupling (D = 50 nm and P = 300 m).

The blue curve represents the propagative surface plasmon, the grey and dark curves are respectively the first order WP at the glass and water interface. The red curve corresponds to the dispersion curve of LSP. We can see the anti-crossing in continuous green lines (hybrid mode) obtained from Eq. (2). The simulated reflectivity map has been evaluated with a numerical model using a combination of two well-known methods named the Fourier modal method (FMM) and the finite element methods (FEM) [45].

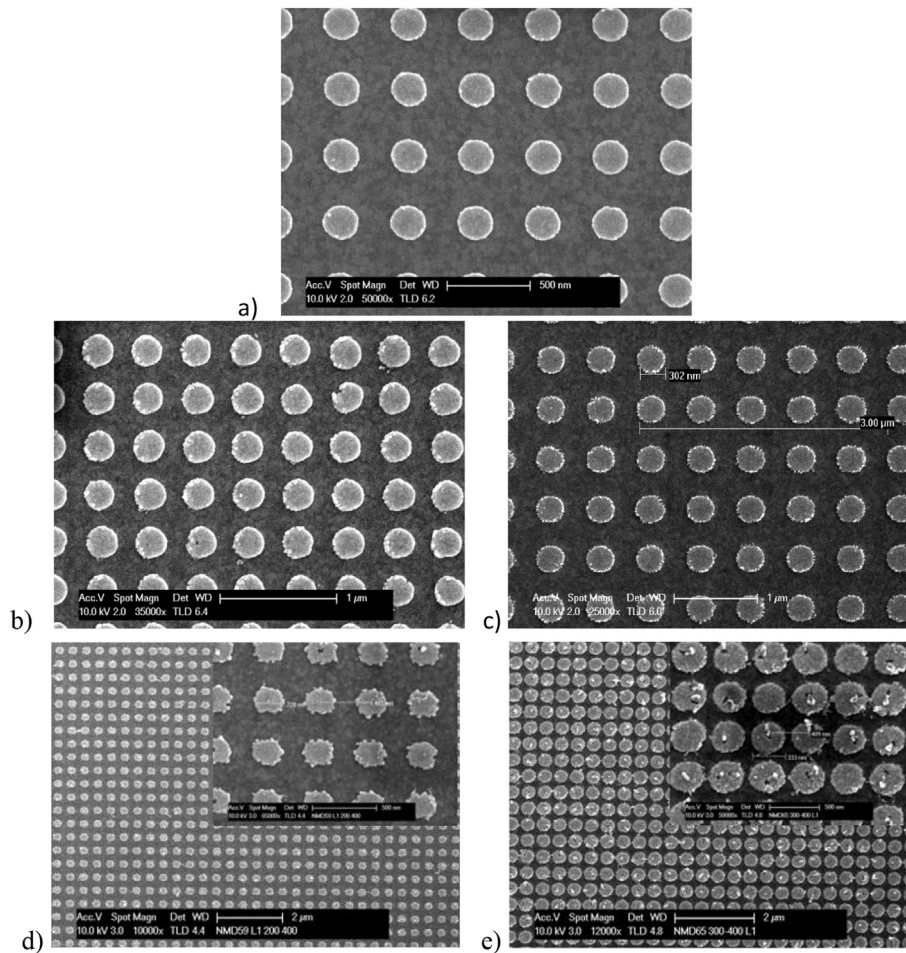


Fig. 4. SEM picture of e-GNGU with $P = 400$ nm and $D = 200$ nm (a), SEM pictures of s-GNGU (b) $P = 400$ nm and $D = 200$ nm, (c) $P = 600$ nm and $D = 300$ nm and SEM pictures of h-GNGU (d) $P = 400$ nm and $D = 210$ nm, (e) $P = 400$ nm and $D = 320$ nm.

Due to experimental constraints (minimum size with UV-NIL sample), our studies focus on 200 nm disks with a period of 400 nm. Four reflectivity maps acquired in water are reported on Fig. 6 in order to compare the simulation (a) with each fabrication techniques, e-beam

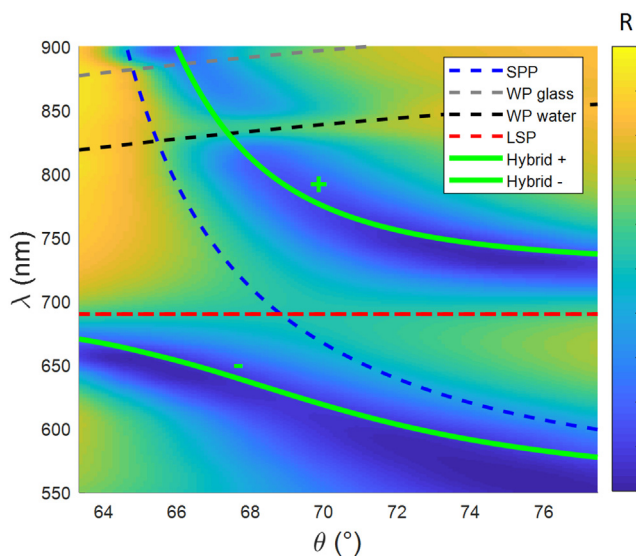


Fig. 5. Normalized angulo-spectral SPR reflectivity map showing the different plasmonics modes ($D = 50$ nm - $P = 300$ nm).

lithography (b), soft (c), and hard UV-NIL (d) for 200 nm disk arrays on gold film. The two branches of hybrid mode (green) are reported on each map as the localized surface plasmon (red) and the 2nd order of Wood-Plasmon anomalies at two interfaces (black).

First, we can note a good agreement between each reflectivity map. Each plasmonic modes expected are present. Nevertheless, some difference in contrast (strength of coupling) and position are observable.

Due to the higher roughness observed on the nanostructures done by soft and hard UV-NIL, the response of localized surface plasmon is modified. This roughness leads to a degradation of coupling by a mean effect of each nanoparticles. Thus, the contrast is lower for soft and hard UV-NIL maps (c and d). To see the modes easily, the scale has been set to 0.5 for the map (c).

Moreover, the widening of the resonance (Hybrid mode +) observed for (c) map can be explained by the presence of small variations of the period within the sample. Indeed, due to the elasticity of the mold in PDMS, the periodicity of the array can be slightly modified locally [39]. As propagation length of propagative surface plasmon is in the micrometric range, these variations of periods will lead to a widening of the resonance.

Nevertheless, we can clearly discern the different resonances. Regarding the map obtained with a sample made by “Hard UV-NIL”, it has a higher contrast and a better finesse, indicating a better definition of nanostructures. In this continuity, the nanostructures realized by e-beam lithography are well defined and the results correspond to the simulation.

Other parameters such as diameter, height and periods have an influence on the position of the superior branch of hybrid mode by

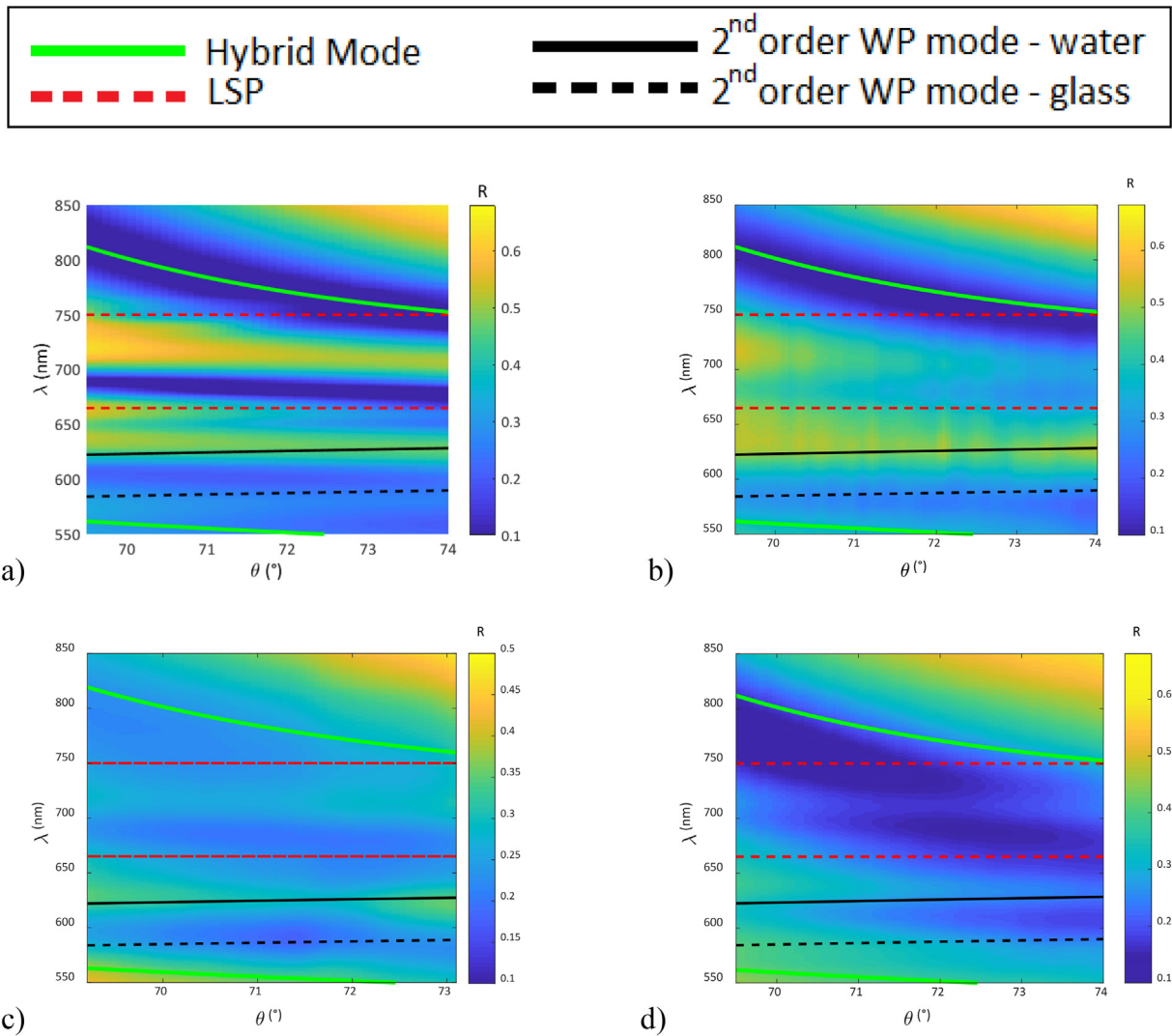


Fig. 6. Reflectivity map of nanodisks ($D = 200$ nm and $P = 400$ nm) on gold layer. Comparison between a simulated map (a) and experimental maps of samples done by three lithographic methods: e-beam lithography (b), soft UV-NIL (c) and hard UV-Nil (d).

modifying the strength of coupling [32,33,44]. An interesting aspect not reported until now, is the effect of the sidewall of nanostructures. Fig. 7 shows the impact of sidewalls angle on plasmonic modes. Modification of the shape of nanostructure induces a shift of the superior branch of hybrid mode of several tens of nanometers. This effect contributes to the difference observed inside the four maps of Fig. 6 and in particular for soft and hard UV-NIL measures. A cross-section of the reflectivity map taken at 71° (Fig. 7a) shows a notable difference in the position of the hybrid mode resonance (branch +) between the different samples (e-beam, soft UV-NIL and hard UV-NIL) in comparison with the ideal sample. In particular, a blue shift is observed in all cases. To explain this blue shift, a simulation considering a sidewall angle has been done (Fig. 7b). Starting from a perfect cylinder to a 45° sidewall, we observed a blue shift of the last resonance similar to the behavior observed experimentally. As previously described, a modification of the mode coupling strength induces a blue shift. As expected, the e-GNGU sample has the position of its last resonance closest to that of an ideal structure. Controlling the sidewalls' slope of a structure at this scale remains an interesting challenge to optimize the plasmonic effects and this numerical simulation explains difference between experiments (with small defects, variations of the shape) and classical numerical simulation based on perfect nanostructures.

3.1.2. SPRI and SERS sensing performances

To measure the sensitivity of these samples to a step of index and to the adsorption of a biolayer on the nanostructures, a sucrose solution and a solution of bovine album serum (BSA) were used. For each experiment, reference was taken with pure water. Results are shown in Table 1. The spectral shift for a modification of the refractive index is significantly lower for gold nanostructure arrays compared to a gold film. The environment sensitivity defined as $S_{\Delta n} = \Delta\lambda / \Delta n$ is around $2 \cdot 10^3$ nm/RIU (Refractive Index Unit) where $\Delta\lambda$ is the spectral shift, Δn is the variation of the refractive index. This is coherent with the presence of the gold nanostructures with a stronger confinement of the electromagnetic field in the vicinity of the surface compared to a continuous gold film. For BSA adsorption, $S_{\Delta n_{bsa}} = \Delta\lambda / \Delta n_{bsa}$ is defined as the spectral shift for a given $\Delta n_{bsa} = 1$ nm thickness of BSA layer. All samples show a similar sensitivity for the detection of BSA, even in the case of hard UV-NIL process.

3.1.3. SERS experiment

To characterize the performance of the different substrates as a SERS sensor [33,34], measurements were performed on several nanostructured areas functionalized by thiophenol molecules with a XploRA spectrophotometer (Horiba Scientific). Characteristic peaks of thiophenol

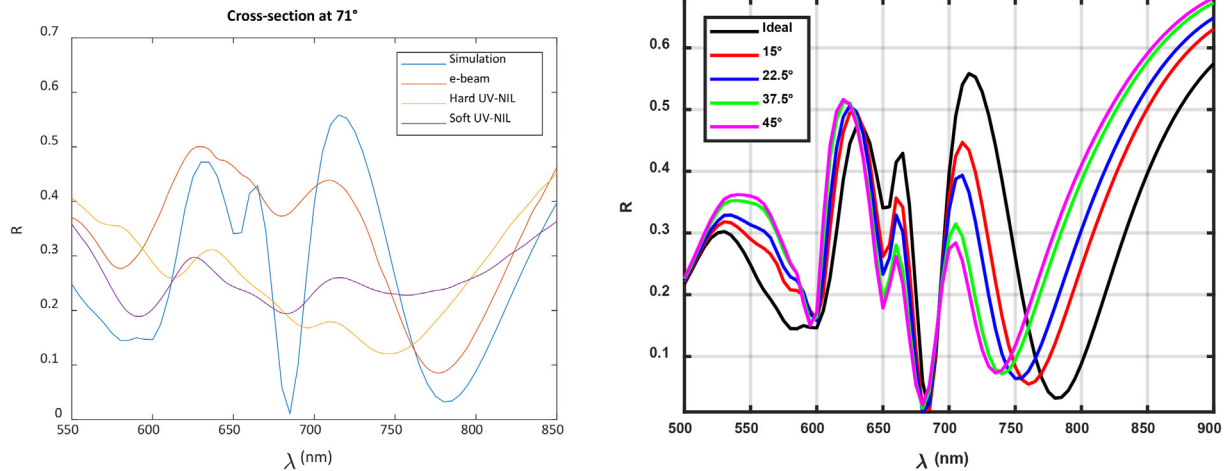


Fig. 7. (a) Cross-section of SPR measurement at 71° for samples done by e-beam, soft and hard UV-NIL in regard of the simulation. (b) Impact of variation of sidewall of nanostructure on SPR profiles at 71° for $D = 200$ and $P = 400$ nm.

molecules are at 419, 1000, 1075, 1575 cm^{-1} for a 660 nm excitation laser. SERS signal was collected in a backscattering configuration and SERS spectra were recorded with a spectral resolution under 4 cm^{-1} . We reported on Fig. 8 the SERS spectra for e-beam lithography, soft, and hard UV-NIL samples.

Enhancement factor is defined by the following equation:

$$EF = \frac{I_{SERS}}{I_{Raman}} \times \frac{N_{Raman}}{N_{SERS}}$$

with I_{SERS}/I_{Raman} are respectively the SERS and Raman intensities. N_{Raman}/N_{SERS} are defined as the number of excited molecules in Raman and SERS experiments. N_{Raman} is estimated to 4.22×10^{15} from the Ref. [46]. N_{SERS} is obtained from: $N_{SERS} = N_A \times S_{collected} \times \sigma_{surf} \times \frac{S_{structure}}{P^2}$ where N_A correspond to the Avogadro's number (mol^{-1}), $S_{collected}$ the illuminated area ($\sim 7 \mu\text{m}^2$), σ_{surf} is the surface coverage of thiophenol molecules with a value of 0.544 nmol/cm^2 [47], $S_{structure}$ is the sum of top and lateral surface of nanodisks. Finally, P is the period of the array. SERS EF are around 4.2×10^6 , 2.6×10^6 and 1.5×10^6 respectively for e-beam sample, soft UV-NIL and hard UV-NIL samples for the characteristic peak at 1575 cm^{-1} (see Table 1). The order of magnitude of 10^6 agrees with previous characterization of samples done by e-beam lithography [33,34] or soft nanoimprint lithography on SiO₂ sol-gel [48]. The difference and lower value for NIL samples can be explained by a modification of the shape of nanostructures and small variations of periods in comparison with e-beam sample. As described for the SPR measurement, the same parameters affecting plasmonic properties decrease SERS performance. These defects induce a lower electromagnetic field as reported for two side wall (0° and 22.5°) in the Fig. 9. A ratio around 2 is obtained between them (ideal and 22.5°) and a ratio of 2.9 for another configuration (ideal and 37.5°) corresponding respectively at side angles observed for soft UV-NIL and hard UV-NIL. These ratios are close and follow the

Table 1
Results of SPRI and SERS measurement for the three lithography methods (e-beam, soft and hard UV-NIL).

Technique	Parameters	SPRI		SERS
		$S_{\Delta bsa}$ (nm/nm)	$S_{\Delta n}$ (nm/RIU)	Enhancement factor (EF)
e-beam lithography	$D = 200$ nm $P = 400$ nm	4 ± 1	2300	4.2×10^6
Soft UV-NIL		4 ± 1	2124	2.6×10^6
Hard UV-NIL		5 ± 2	2000	1.5×10^6
none	30 nm gold film	4.2 ± 1	5420	Not applicable

same behaviour to the SERS EF ratio obtained between e-beam/Soft UV-NIL (1.6) and e-beam/hard UV-NIL samples (2.8). Nevertheless, the SERS intensities obtained from NIL samples is still acceptable.

4. Conclusion

This paper compares different plasmonic substrates realized by three lithography methods: e-beam, soft, and hard UV-NIL. The first technique is well known as a reference to fabricate nanostructured sample and the two others allow faster, larger and cheaper fabrication as required for industrial applications but at the possible cost of lower quality. In our case, samples are composed of gold nanostructures on gold film that support both SPP and LSP plasmonic modes which coupling results in a hybrid mode with particularly interesting sensing properties. Numerical simulations have investigated the impact of inherent sidewall tilt on the plasmonic properties and in particular on the position of the hybrid mode resonance. The consequences of this defect for different sensing applications, depending on the fabrication technique, were experimentally quantified by measuring and comparing the SPR and SERS signals obtained with these substrates. A blue spectral shift was predicted, attributed to a difference of coupling strength between SPP and LSP. Experimentally observed in the presence of a sidewall on the nanostructure, this blue shift was typically of the

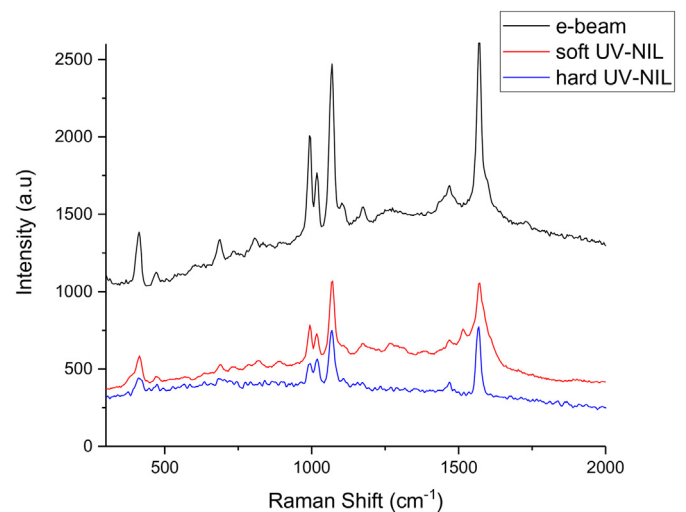


Fig. 8. SERS Intensities of disks ($D = 200$ nm $P = 400$ nm) on gold film for e-beam, soft, and hard UV-NIL samples functionalized with thiophenol molecules.

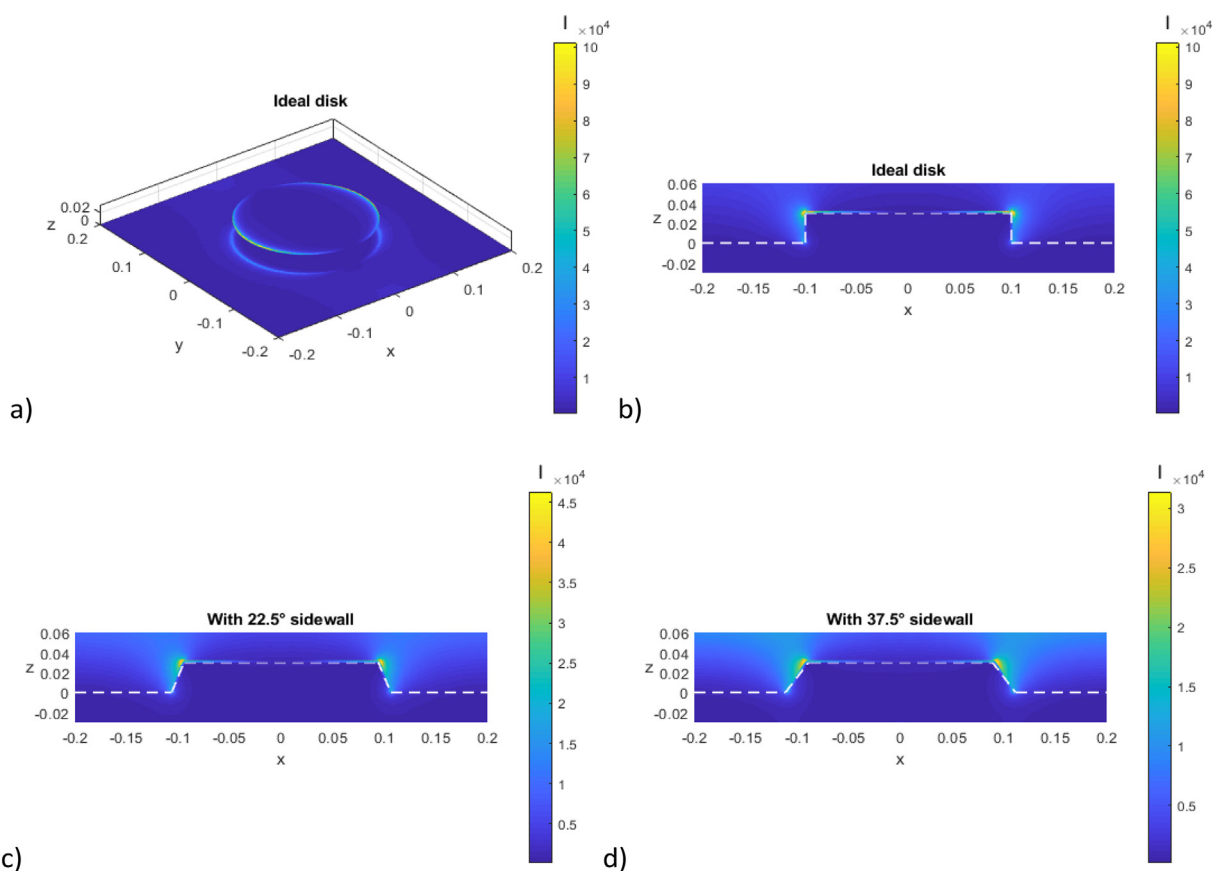


Fig. 9. Intensity of the electromagnetic field maps for perfect disk and two sidewalls of nanostructures, a (ideal, vertical slope), b) cross-section for ideal case, cross-section for sidewall of 22.5° (c) and sidewall of 37.5° (d) with guidelines.

order of 1 nm° (although not perfectly linear) for SPR measurement at an excitation angle of 71° . This can explain some of the differences between ideal simulation and reality as observed in many plasmonic experiments. For SERS measurement, we have shown a great correlation between experimental SERS intensities and electromagnetic field maps with appropriate sidewalls. The presence of sidewalls induces a diminution of the intensity of the electromagnetic field over the nanostructures (close to 0.08°), resulting in a lower sensitivity. Altogether, such control of the sidewall remains a great challenge in nanofabrication but can be anticipated and used to tune the coupling between plasmonic modes at the position of working wavelength.

Conflict of interest

The authors declare that they have no known competing financial interests or personal relationships that could have appeared to influence the work reported in this paper.

Acknowledgements

This work was done with the CTU IEF-MINERVE facility and partly supported by the RENATECH network and the General Council of Essonne. Moreover, the authors acknowledge ANR P2N (ANR-12-125 NANO-0016) and the support of the French Government for partial funding of the project in which this work took place. LN2 is an international laboratory (Unité Mixte Internationale UMI 3463) jointly managed by French CNRS and the Université de Sherbrooke as well as Université de Lyon (ECL, INSA de Lyon, CPE) and the Université Grenoble Alpes (UGA). LN2 is also financially supported by FRQNT in Québec.

References

- [1] J. Homola, S.S. Yee, G. Gauglitz, Surface plasmon resonance sensors: review, *Sensors Actuators B Chem.* 54 (1) (1999) 3–15, [https://doi.org/10.1016/S0925-4005\(98\)00321-9](https://doi.org/10.1016/S0925-4005(98)00321-9).
- [2] B. Sharma, R.R. Frontiera, A.-I. Henry, E. Ringe, R.P. Van Duyne, SERS: materials, applications, and the future, *Mater. Today* 15 (1) (2012) 16–25, [https://doi.org/10.1016/S1369-7021\(12\)70017-2](https://doi.org/10.1016/S1369-7021(12)70017-2).
- [3] R.A. Halvorson, P.J. Vikesland, Surface-enhanced Raman spectroscopy (SERS) for environmental analyses, *Environ. Sci. Technol.* 44 (20) (2010) 7749–7755, <https://doi.org/10.1021/es101228z>.
- [4] F. Le, D.W. Brandl, Y.A. Urzhumov, H. Wang, J. Kundu, N.J. Halas, J. Aizpurua, P. Nordlander, Metallic nanoparticle arrays: a common substrate for both surface-enhanced Raman scattering and surface-enhanced infrared absorption, *ACS Nano* 2 (4) (2008) 707–718, <https://doi.org/10.1021/nn800047e>.
- [5] J. Dostalek, W. Knoll, Biosensors based on surface plasmon-enhanced fluorescence spectroscopy (Review), *Biointerphases* 3 (3) (2008) FD12–FD22, <https://doi.org/10.1116/1.2994688>.
- [6] D. Nedelkov, Integration of SPR biosensors with mass spectrometry (SPR-MS), *Methods Mol. Biol.* (2010) 261–268, https://doi.org/10.1007/978-1-60761-670-2_18.
- [7] X. Chen, K.M. Shakesheff, M.C. Davies, J. Heller, C.J. Roberts, S.J.B. Tendler, P.M. Williams, Degradation of a thin polymer film studied by simultaneous in situ atomic force microscopy and surface plasmon resonance analysis, *J. Phys. Chem.* 99 (29) (1995) 11537–11542, <https://doi.org/10.1021/j100029a036>.
- [8] A. Sonato, M. Agostini, G. Ruffato, E. Gazzola, D. Liuni, G. Greco, M. Travagliati, M. Cecchini, F. Romanato, A surface acoustic wave (SAW)-enhanced grating-coupling phase-interrogation surface plasmon resonance (SPR) microfluidic biosensor, *Lab Chip* 16 (7) (2016) 1224–1233, <https://doi.org/10.1039/c6lc00057f>.
- [9] J.-M. Friedt, L.A. Francis, Combined surface acoustic wave and surface plasmon resonance measurement of collagen and fibrinogen layer physical properties, *Sens. Bio-Sens. Res.* 11 (2016) 60–70, <https://doi.org/10.1016/j.sbsr.2016.05.007>.
- [10] S.A. Meyer, B. Auguie, E.C.L. Ru, P.G. Etchegoin, Combined SPR and SERS microscopy in the Kretschmann configuration, *J. Phys. Chem. A* 116 (3) (2012) 1000–1007, <https://doi.org/10.1021/jp2107507>.
- [11] S.A. Meyer, E.C.L. Ru, P.G. Etchegoin, Combining surface plasmon resonance (SPR) spectroscopy with surface-enhanced Raman scattering (SERS), *Anal. Chem.* 83 (6) (2011) 2337–2344, <https://doi.org/10.1021/ac103273r>.
- [12] Y. Liu, S. Xu, B. Tang, Y. Wang, J. Zhou, X. Zheng, B. Zhao, W. Xu, Note: Simultaneous measurement of surface plasmon resonance and surface-enhanced Raman scattering, *Rev. Sci. Instrum.* 81 (3) (2010), 036105, <https://doi.org/10.1063/1.3321313>.

- [13] P.I. Nikitin, A.A. Beloglazov, M.V. Valeiko, J.A. Creighton, J.D. Wright, Silicon-based surface plasmon resonance combined with surface-enhanced Raman scattering for chemical sensing, *Rev. Sci. Instrum.* 68 (6) (1997) 2554–2557, <https://doi.org/10.1063/1.1148160>.
- [14] B.D. Gates, Q. Xu, M. Stewart, D. Ryan, C.G. Willson, G.M. Whitesides, New approaches to nanofabrication: molding, printing, and other techniques, *Chem. Rev.* 105 (4) (2005) 1171–1196, <https://doi.org/10.1021/cr030076o>.
- [15] Q. Yu, S. Braswell, B. Christin, J. Xu, P.M. Wallace, H. Gong, D. Kaminsky, Surface-enhanced Raman scattering on gold quasi-3D nanostructure and 2D nanohole arrays, *Nanotechnology* 21 (35) (2010) 355.301, <https://doi.org/10.1088/0957-4484/21/35/355301>.
- [16] Q. Yu, P. Guan, D. Qin, G. Golden, P.M. Wallace, Inverted size-dependence of surface-enhanced Raman scattering on gold nanohole and nanodisk arrays, *Nano Lett.* 8 (7) (2008) 1923–1928, <https://doi.org/10.1021/nl0806163>.
- [17] P. Zhang, S. Yang, L. Wang, J. Zhao, Z. Zhu, B. Liu, J. Zhong, X. Sun, Large-scale uniform Au nanodisk arrays fabricated via x-ray interference lithography for reproducible and sensitive SERS substrate, *Nanotechnology* 25 (24) (2014), 245301. <https://doi.org/10.1088/0957-4484/25/24/245301>.
- [18] Y.-Y. Lin, J.-D. Liao, Y.-H. Ju, C.-W. Chang, A.-L. Shiau, Focused ion beam-fabricated Au micro/nanostructures used as a surface enhanced Raman scattering-active substrate for trace detection of molecules and influenza virus, *Nanotechnology* 22 (18) (2011), 185308. <https://doi.org/10.1088/0957-4484/22/18/185308>.
- [19] J.P. Camden, J.A. Dieringer, J. Zhao, R.P.V. Duyne, Controlled plasmonic nanostructures for surface-enhanced spectroscopy and sensing, *Acc. Chem. Res.* 41 (12) (2008) 1653–1661, <https://doi.org/10.1021/ar800041s>.
- [20] J.-F. Bryche, A. Tsigara, B. Bélier, M.L. de la Chapelle, M. Canva, B. Bartenlian, G. Barbillon, Surface enhanced Raman scattering improvement of gold triangular nanoprisms by a gold reflective underlayer for chemical sensing, *Sensors Actuators B Chem.* 228 (2016) 31–35, <https://doi.org/10.1016/j.snb.2016.01.018>.
- [21] V.N. Truskett, M.P.C. Watts, Trends in imprint lithography for biological applications, *Trends Biotechnol.* 24 (7) (2006) 312–317, <https://doi.org/10.1016/j.tibtech.2006.05.005>.
- [22] H. Schiff, Nanoimprint lithography: an old story in modern times? A review, *J. Vac. Sci. Technol. B* 26 (2) (2008) 458, <https://doi.org/10.1116/1.2890972>.
- [23] G. Barbillon, F. Hamouda, S. Held, P. Gogol, B. Bartenlian, Gold nanoparticles by soft UV nanoimprint lithography coupled to a lift-off process for plasmonic sensing of antibodies, *Microelectron. Eng.* 87 (5–8) (2010) 1001–1004, <https://doi.org/10.1016/j.mee.2009.11.114>.
- [24] F. Hamouda, H. Sahaf, S. Held, G. Barbillon, P. Gogol, E. Moyen, A. Aassime, J. Moreau, M. Canva, J.-M. Lourtioz, M. Hanbücken, B. Bartenlian, Large area nanopatterning by combined anodic aluminum oxide and soft UVNIL technologies for applications in biology, *Microelectron. Eng.* 88 (8) (2011) 2444–2446, <https://doi.org/10.1016/j.mee.2011.02.013>.
- [25] A. Finn, B. Lu, R. Kirchner, X. Thrun, K. Richter, W.-J. Fischer, High aspect ratio pattern collapse of polymeric UV-nano-imprint molds due to cleaning, *Microelectron. Eng.* 110 (2013) 112–118, <https://doi.org/10.1016/j.mee.2013.02.065>.
- [26] Y.Y. Huang, W. Zhou, K.J. Hsia, E. Menard, J.-U. Park, J.A. Rogers, A.G. Alleyne, Stamp Collapse in Soft Lithography, *Langmuir* 21 (17) (2005) 8058–8068, <https://doi.org/10.1021/la0502185>.
- [27] M.-E. Vlachopoulou, P.S. Petrou, S.E. Kakabakos, A. Tserepi, K. Beltsios, E. Gogolides, Effect of surface nanostructuring of PDMS on wetting properties, hydrophobic recovery and protein adsorption, *Microelectron. Eng.* 86 (4–6) (2009) 1321–1324, <https://doi.org/10.1016/j.mee.2008.11.050>.
- [28] K. Ma, J. Rivera, G.J. Hirasaki, S.L. Biswal, Wettability control and patterning of PDMS using UVozone and water immersion, *J. Colloid Interface Sci.* 363 (1) (2011) 371–378, <https://doi.org/10.1016/j.jcis.2011.07.036>.
- [29] M. Bender, M. Otto, B. Hadam, B. Vratzov, B. Spangenberg, H. Kurz, Fabrication of nanostructures using a UV-based imprint technique, *Microelectron. Eng.* 53 (1–4) (2000) 233–236, [https://doi.org/10.1016/S0167-9317\(00\)00304-X](https://doi.org/10.1016/S0167-9317(00)00304-X).
- [30] M. Sarkar, M. Besbes, J. Moreau, J.-F. Bryche, A. Olivéro, G. Barbillon, A.-L. Coutrot, B. Bartenlian, M. Canva, Hybrid plasmonic mode by resonant coupling of localized plasmons to propagating plasmons in a Kretschmann configuration, *ACS Photonics* 2 (2) (2015) 237–245, <https://doi.org/10.1021/ph500351b>.
- [31] J.-F. Bryche, R. Gillibert, G. Barbillon, P. Gogol, J. Moreau, M. Lamy De La Chapelle, B. Bartenlian, M. Canva, Plasmonic enhancement by a continuous gold underlayer: application to SERS sensing, *Plasmonics* 11 (2) (2016) 601–608, <https://doi.org/10.1007/s11468-015-0088-y>.
- [32] J.-F. Bryche, R. Gillibert, G. Barbillon, M. Sarkar, A.-L. Coutrot, F. Hamouda, A. Aassime, J. Moreau, M.L. de la Chapelle, B. Bartenlian, M. Canva, Density effect of gold nanodisks on the SERS intensity for a highly sensitive detection of chemical molecules, *J. Mater. Sci.* 50 (20) (2015) 6601–6607, <https://doi.org/10.1007/s10853-015-9203-x>.
- [33] R.L. Bates, P.L. Stephan Thamban, M.J. Goekner, L.J. Overzet, Silicon etch using SF₆/C₄F₈/Ar gas mixtures, *J. Vac. Sci. Technol. A* 32 (4) (2014) 41302, <https://doi.org/10.1116/1.4880800>.
- [34] K. Mohamed, M.M. Alkai, R.J. Blaikie, Fabrication of three dimensional structures for an UV curable nanoimprint lithography mold using variable dose control with critical-energy electron beam exposure, *J. Vac. Sci. Technol. B* 25 (6) (2007) 2357, <https://doi.org/10.1116/1.2794317>.
- [35] P. Roca-Cusachs, F. Rico, E. Martnez, J. Toret, R. Farré, D. Navajas, Stability of microfabricated high aspect ratio structures in poly(dimethylsiloxane), *Langmuir* 21 (12) (2005) 5542–5548, <https://doi.org/10.1021/la046931w>.
- [36] F. Hamouda, G. Barbillon, S. Held, G. Agnus, P. Gogol, T. Maroutian, S. Scheuring, B. Bartenlian, Nanoholes by soft UV nanoimprint lithography applied to study of membrane proteins, *Microelectron. Eng.* 86 (4–6) (2009) 583–585, <https://doi.org/10.1016/j.mee.2008.11.086>.
- [37] F. Hamouda, A. Aassime, H. Bertin, P. Gogol, B. Bartenlian, B. Dagens, Tunable diffraction grating in flexible substrate by UV-nanoimprint lithography, *J. Micromech. Microeng.* 27 (2) (2017) 25017, <https://doi.org/10.1088/1361-6439/aa5404>.
- [38] D. Truffier-Boutry, R. Galand, A. Beaurain, A. Francone, B. Pelissier, M. Zelsmannet, J. Boussey, Mold cleaning and fluorinated anti-sticking treatments in nanoimprintlithography, *Microelectron. Eng.* 86 (4–6) (2009) 669–672, <https://doi.org/10.1016/j.mee.2009.01.065>.
- [39] M. Nakkach, A. Duval, B. Ea-Kim, J. Moreau, M. Canva, Angulo-spectral surface plasmon resonance imaging of nanofabricated grating surfaces, *Opt. Lett.* 35 (13) (2010) 2209, <https://doi.org/10.1364/ol.35.002209>.
- [40] L. Novotny, Strong coupling, energy splitting, and level crossings: a classical perspective, *Am. J. Phys.* 78 (11) (2010) 1199–1202, <https://doi.org/10.1119/1.3471177>.
- [41] M. Sarkar, J.-F. Bryche, J. Moreau, M. Besbes, G. Barbillon, B. Bartenlian, M. Canva, Generalized analytical model based on harmonic coupling for hybrid plasmonic modes: comparison with numerical and experimental results, *Opt. Express* 23 (21) (2015), 27376. <https://doi.org/10.1364/oe.23.027376>.
- [42] J.P. Hugonin, M. Besbes, P. Lalanne, Hybridization of electromagnetic numerical methods through the G-matrix algorithm, *Opt. Lett.* 33 (14) (2008) 1590, <https://doi.org/10.1364/OL.33.001590>.
- [43] M. Cottat, N. Lidji-Guigui, I. Tijunelyte, G. Barbillon, F. Hamouda, P. Gogol, A. Aassime, J.M. Lourtioz, B. Bartenlian, M. Lamy De La Chapelle, Soft UV nanoimprint lithography-designed highly sensitive substrates for SERS detection, *Nanoscale Res. Lett.* 9 (2014) 623, <https://doi.org/10.1186/1556-276x-9-623>.
- [44] D.A. Stern, E. Wellner, G.N. Salaita, L. Laguren-Davidson, F. Lu, N. Batina, D.G. Frank, D.C. Zapien, N. Walton, A.T. Hubbard, Adsorbed thiophenol and related compounds studied at platinum(111) electrodes by EELS, Auger spectroscopy, and cyclic voltammetry, *J. Am. Chem. Soc.* 110 (1988) 4887, <https://doi.org/10.1021/ja00223a003>.
- [45] F. Hamouda, J.-F. Bryche, A. Aassime, E. Maillart, V. Gâté, S. Zanetini, J. Ruscica, D. Turover, B. Bartenlian, Soft nanoimprint lithography on SiO₂ sol-gel to elaborate sensitive substrates for SERS detection, *AIP Adv.* 7 (12) (2017), 125125. <https://doi.org/10.1063/1.5004122>.